Band structure and charge control studies of *n*- and *p*-type pseudomorphic modulation-doped field-effect transistors

Mark Jaffe and Jasprit Singh
Center for High Frequency Microelectronics, Department of Electrical Engineering and Computer Science, The University of Michigan, Ann Arbor, Michigan 48109

(Received 16 December 1987; accepted for publication 31 August 1988)

We present results of a numerical formalism developed to address the band structure and the charge control problem in pseudomorphic *n*- and *p*-type modulation-doped field-effect transistors (MODFETs), which are created by adding excess indium in the active channel region. For *n*-type structures, the tight-bonding formalism is used to study the effect of strain on the crystal electronic properties. A finite-difference technique to solve the Schrödinger equation simultaneously with the Poisson equation is used to model the MODFET. The enhanced performance in *n*-type pseudomorphic devices has been shown to be primarily due to better charge confinement. Results are also presented as a function of channel strain. For *p*-type structures, the Kohn–Luttinger formulation is used together with deformation potential theory to describe the hole states. Significant reductions in the mass of the hole gas due to biaxial compressive strain are demonstrated, suggesting dramatic potential improvement in the operation characteristics of *p*-type pseudomorphic devices. As an application of the formalism, a comparison of pulse and uniform doping in the barrier region is carried out. The improvement in carrier transfer efficiency and the potential reduction of gate leakage current are discussed.

I. INTRODUCTION

Strained channel or pseudomorphic modulation-doped field-effect transistors (MODFETs) have been receiving a lot of attention recently for application as high-speed/high-frequency devices. These devices also offer well-controlled systems for studying optical, electronic, and transport properties in strained systems. Studies of strained MODFETs are motivated by a number of potential advantages, including (i) the potential to avoid the *D-X* center related problems which plague the cryogenic performance of GaAs/$Al_{0.3}Ga_{0.7}As$ MODFET[1] by using the $In_xGa_{1-x}As$/$Al_{0.15}Ga_{0.85}As$ system,[2] (ii) higher band discontinuities which could yield greater sheet charge densities and better carrier confinement by adding excess In in the channel of both the GaAs/AlGaAs and $In_{0.53}Ga_{0.47}As/In_{0.52}Al_{0.48}As$ systems, and (iii) lowering of carrier masses due to the added In in the case of *n*-type MODFETs and due to the band decoupling caused by biaxial compressive strain in the case of *p*-type MODFETs. Many of these advantages appear to have been realized, and the *n*-type strained devices have shown improved performance which is related to higher mobility and better carrier confinement. The *p*-type MODFET has shown remarkably improved performance which appears to be related to the lower carrier mass due to the strain in the channel. The need for superior hole transport properties exists for both *p*-type MODFETs (for complementary logic) and for *npn* heterojunction bipolar transistors. Jones *et al.*[3] have shown that hole masses can be reduced by biaxial compressive strain. Hinckley and Singh[4] have shown significant improvements in the theoretical transport properties of pseudomorphic *p*-type material. Drummond *et al.*[5] and Lee *et al.*[6] find improved device performance in strained *p*-type MODFETs.

To fully exploit the potential of strained MODFETs, one needs to develop an accurate formalism to study the channel material properties as well as the charge control properties of both *n*- and *p*-type devices. Such a model would require the self-consistent solution of the Schrödinger equation and the Poisson equation in the presence of strain. An accurate model must be able to solve the Schrödinger equation with an arbitrarily shaped potential well, as well as being able to include the effects of different material parameters across boundaries. This precludes the use of variational techniques or triangular well assumptions which are popularly used in MODFET charge control studies. It is also important to consider the mixing between light-hole (LH) states and heavy-hole (HH) states explicitly when simulating the *p*-type MODFET since this interaction qualitatively changes the properties of the hole gas. We have used a numerical finite-difference eigenvalue solution to handle the Schrödinger equation for *n*- and *p*-type systems.

We have applied our formalism not only to develop an understanding of the carrier properties, masses, subband energies, and occupations, etc., of MODFETs, but also to a study of the effects of doping distribution in the barrier. The enhanced transfer efficiency which is found in the case of pulse doping is discussed. Also, advantages due to potentially much lower gate leakage current are identified on the basis of the band bending. Further, we find that if modeled accurately, the shape of the conduction band yields a quantum well in the barrier region which has its own confined electronic subband levels. Thus, the device has two quantum wells—one in the barrier and one below the heterointerface.

In the next section, we describe the modeling formalism for the *n*- and *p*-type devices. Results of the formalism are presented in Sec. III, and we conclude in Sec. IV.

 0021-8979/89/010329-10$02.40

II. MODELING FORMALISM

The general structure of the pseudomorphic, or strained channel, MODFET is shown in Fig. 1. Excess In is added in the channel layer where the two-dimensional electron (hole) gas is formed. The excess In creates a lattice mismatch between the channel layer and the rest of the device. The lattice mismatch, which results in a biaxial compressive strain, alters the physical properties of the semiconductor material. Before the pseudomorphic MODFET properties can be understood, it is important to understand the band structure of the strained region. Once the band structure and other material properties of the pseudomorphic layer are known, one can proceed with a simulation of the device. In our simulation, we solve the Schrödinger equation self-consistently with the Poisson equation. In Fig. 2, we depict the general flowchart of our approach to n- and p-type MODFET simulation. We now briefly describe the components of our formalism.

A. Material parameters of pseudomorphically strained semiconductors.

A general charge control model for a semiconductor device begins with the material band gap, the effective mass, and other similar material properties. For unstrained bulk semiconductors, these parameters are readily available from many sources both theoretical and experimental. Since it is known that strain will alter these basic material properties, one must first establish values for these parameters in the strained semiconductor. At present, there has been some experimental work on the band gaps[7] and effective masses[8] in some strained systems, however, full data are not yet available. For this reason, we have developed a model for the electronic band structure which incorporates strain.

We employ the tight-binding method (TBM) in order to model the carrier masses in the strained n-type channel. The band structure is developed first for the unstrained semiconductor material by carefully fitting the band gap, effective masses, and intervalley separations to measured data. The effects of spin-orbit interaction are included in the tight-binding formalism.[9] The virtual crystal approximation is employed to model alloys by averaging the tight-binding matrix elements. This yields a set of tight-binding matrix elements (and spin-orbit coupling parameters) which fairly accurately describe the band structure to about 1 eV away from the band gap for both the electron and hole states. After the tight-binding parameter set for an unstrained semiconductor is developed, the effects of strain on the tight binding band structure are considered. A scaled square law rule is used to alter the tight-binding matrix elements with the change in atomic separation. Our formalism uses the following relation:

$$E_{\mu,\mu'}(r_0+\delta r)=E_{\mu,\mu'}(r_0)\Big/\left[1+\alpha\left(\frac{2\delta r}{r_0}+\frac{\delta r^2}{r_0^2}\right)\right], \quad (1)$$

to describe the effect of strain on the tight binding parameters $E_{\mu,\mu'}$. Here μ and μ' stand for atomic orbitals (s, p_x, p_y, p_z) at sites which in the absence of strain are separated by a distance r_0. δr is the change in the atomic spacing and α is a fitting factor used to match the calculated deformation potentials for hydrostatic and biaxial deformation to measured values. Different values for α were used for first and second nearest-neighbor interactions. This expression, when incorporated into the tight-binding formalism, allows one to describe the energy band structure under arbitrary strain conditions.

Using this formalism, we can model the band structure of the strained channel material if it is known how the channel material absorbs the strain of the lattice mismatch. We employ the pseudomorphic approximation for strain incorporation in the channel material. According to this approximation, the lattice constant of the regions matched to the substrate is unaffected. In the nonmatched region, the parallel lattice constant is forced to take on the value of the lattice constant of the substrate, while the perpendicular lattice constant of the nonmatched material is then altered according to the Poisson effect. This condition allows lattice coherency to be maintained and a crystal to exist without lattice dislocations. Such an approximation is expected to be valid if the strained layer thickness is below some critical thickness which is determined by material parameters. Thus, the parallel and perpendicular lattice constants of the strained channel become

$$a_{\parallel}^{c}=a_0^{s}=(1+\epsilon)a_0^{c}, \quad (2)$$

$$a_{\perp}^{c}=(1-\sigma^{c}\epsilon)a_0^{c}, \quad (3)$$

where a_0 represents an unstrained material lattice constant, the superscript c denotes the pseudomorphically strained channel material, the superscript s denotes the substrate ma-

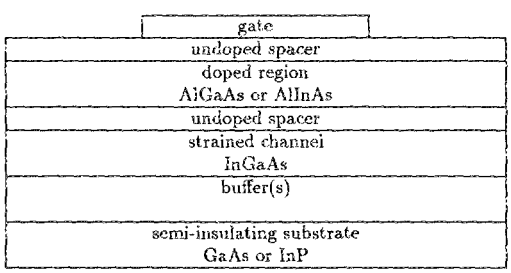

FIG. 1. General structure of the pseudomorphic MODFET.

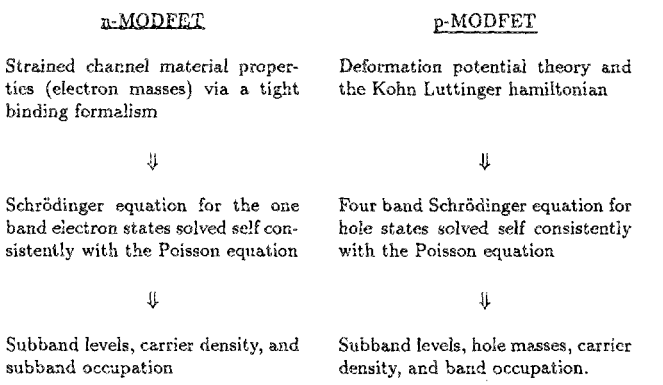

FIG. 2. Flowchart depicting the modeling procedure for n- and p-type pseudomorphic MODFETs.

terial, ϵ is the amount of lattice mismatch and is defined by Eq. (2), and σ is the channel material Poisson ratio.

This model was used to calculate the band structure of $In_xGa_{1-x}As$ lattice matched to GaAs, and for $In_{0.53+x}Ga_{0.47-x}As$ lattice matched to InP where $0 \leqslant x \leqslant 0.20$. In Table I we list the calculated band gaps for both the lattice-matched and the pseudomorphically strained channel material of the listed compositions. In Table II, the effective masses are listed. Note that Table II gives values of the effective mass in the parallel and perpendicular directions for the strained channel materials. For unstrained materials, the equal-energy surfaces for the gamma valley are spherical in the materials which we are considering. Strain, however, lowers the symmetry of the crystal and changes the shape of the equienergy surfaces into an ellipsoid. That is, the biaxially strained gamma valley must be characterized by a parallel and a perpendicular effective mass which will, in general, be different. It can be seen from Table II that the perpendicular effective mass tends to saturate as the indium composition (and the strain) increases. The parallel effective mass, however, continues to decrease with excess indium, although it does remain above the unstrained value.

The tight-binding band-structure formalism which we have developed will model the valence-band structure as well as the conduction-band structure. However, a listing of the masses of the hole bands would not serve the same purpose as the list of the electron effective masses did. This is because of the fact that the top of the valence band is doubly degenerate. The top two valence bands, termed the light hole and heavy hole, couple strongly. This coupling, to a large extent, determines the masses of the two states and can be responsible for making the hole bands very nonparabolic. Both strain and the quantum confinement produced in a MODFET will alter the relative positions of the light-and heavy-hole bands. Thus, both strain and confinement can effect the coupling and dramatically alter the hole effective masses. Because of this, one cannot determine the hole effective masses until after the valence-band profile is determined. Since the valence band is dependent upon the hole masses, one is forced to solve for the hole band structure self-consistently with the charge control model instead of *a priori* as is possible in the electron case.

While it would be possible to insert the full tight-binding Hamiltonian into the charge control model as an equation to be solved self-consistently with the Poisson equation, this would create an unmanageably large matrix. Since we were only interested in the topmost hole bands, it is possible to use a reduced basis set. Such a reduced basis is used in the 4×4 Kohn–Luttinger Hamiltonian and is valid for systems such as InGaAs which have large spin-orbit splittings. This Hamiltonian can accurately describe the top of the valence bands and is much smaller than the sp^3 tight-binding Hamiltonian. Thus, we incorporate the Kohn–Luttinger Hamiltonian into our charge control model for p-type MODFETs. This will be described in detail below.

TABLE II. Effective masses in the perpendicular and parallel directions fc pseudomorphically strained channel materials on GaAs and InP substrate

	$In_xGa_{1-x}As$			$In_{0.53+x}Ga_{0.47-x}As$		
x	$m^*_{unstrained}$	$m^*_{\parallel unstrained}$	$m^*_{\perp strained}$	$m^*_{unstrained}$	$m^*_{\parallel strained}$	$m^*_{\perp strained}$
0.00	0.066	0.066	0.066	0.045	0.045	0.045
0.05	0.064	0.065	0.064	0.044	0.044	0.045
0.10	0.062	0.064	0.063	0.042	0.043	0.045
0.15	0.060	0.063	0.063	0.040	0.041	0.044
0.20	0.058	0.062	0.062	0.037	0.039	0.044
0.25	0.056	0.061	0.061	0.035	0.037	0.044
0.30	0.054	0.060	0.061	0.033	0.035	0.043
0.35	0.052	0.058	0.060	0.031	0.033	0.043
0.40	0.050	0.057	0.060	0.028	0.030	0.043
0.45	0.048	0.055	0.060	0.026	0.027	0.042
0.50	0.047	0.054	0.060	...	...	...
0.55	0.045	0.052	0.060	...	...	...
0.60	0.043	0.050	0.060	...	...	...
0.65	0.041	0.048	0.060	...	...	...

TABLE I. Band gaps of pseudomorphically strained channel materials on GaAs and InP substrates derived using tight-binding formalism. The measured band gaps of alloys are usually somewhat lower than the numbers given here because of atomic clustering.

	$In_xGa_{1-x}As$			$In_{0.53+x}Ga_{0.47-x}As$		
x	E_{gap} Unstrained	E_{gap} Strained	Critical thickness	E_{gap} Unstrained	E_{gap} Strained	Critical thickness
0.00	1.454	1.454	∞	0.876	0.876	∞
0.05	1.399	1.416	775	0.822	0.834	843
0.10	1.344	1.377	336	0.768	0.791	366
0.15	1.289	1.339	203	0.714	0.745	222
0.20	1.235	1.299	141	0.660	0.697	154
0.25	1.180	1.259	105	0.606	0.647	115
0.30	1.125	1.218	83.0	0.552	0.595	91.0
0.35	1.071	1.176	67.0	0.499	0.539	74.0
0.40	1.016	1.132	56.0	0.445	0.480	62.0
0.45	0.962	1.086	47.0	0.392	0.418	52.0
0.50	0.908	1.038	41.0	...	...	...
0.55	0.854	0.988	36.0	...	...	...
0.60	0.800	0.935	31.0	...	...	...
0.65	0.746	0.879	28.0	...	...	...

B. The charge control model

Our model solves for the potential profile in a MODFET by self-consistently solving the Schrödinger equation and the Poisson equation. The Schrödinger equation will yield one of the charge terms in the Poisson equation which, in turn, determines the potential profile which is fed back into the Schrödinger equation. An iterative process brings both equations into convergence simultaneously.

The one-dimensional Poisson equation can be written as

$$\frac{\partial^2}{\partial z^2} E_c(z) = -\frac{\rho(z)}{\epsilon(z)}, \tag{4}$$

where E_c is the conduction-band profile in the device, ρ is the charge density, and ϵ is the permittivity which can be changed in different regions of the device to account for different material parameters across interfaces. The charge density $\rho(z)$ is the sum of the doping charge, the free charge, and the quantum-confined charge. This can be written as

$$\rho(z) = q\Big(N_d^*(z) - N_a^*(z) - n_{\text{free}}(z) + p_{\text{free}}(z) - \sum_i n_i \phi_i^*(z)\phi_i(z)\Big), \tag{5}$$

where N_a^* and N_d^* are the effective doping levels, n_{free} and p_{free} are the free-carrier concentrations, and the sum is over i two-dimensionally confined subbands whose normalized envelope functions are ϕ_i and in which the occupation is n_i (or p_i for the hole case). The solution of the Poisson equation is performed by a vectorized Newton's method.

The effective doping levels are the concentration of ionized dopants. It is important to determine the percentage of the dopants which are ionized when, for example, the conduction band dips down close to the Fermi level. When this happens, the donor levels begin to fill. A filled, or unionized, donor site is charge neutral and does not contribute a free electron. Writing

$$N_d^* = N_d(1 - \langle n_d \rangle), \tag{6}$$

where N_d is the total real concentration of donor atoms and $\langle n_d \rangle$ is the average occupation of a donor level. The effective donor concentration can be written as[10]

$$N_d^* = N_d\left(\frac{1}{1 + 2e^{(E_d - E_f)/kT}}\right). \tag{7}$$

Here, E_d is the donor level which is usually at a fixed energy below the conduction band.

In the calculation of the charge density, one must solve the Schrödinger equation to determine the two-dimensionally confined charge profile, and one must also determine the free-charge concentrations. In the absence of a potential well which confines carriers in the z direction, the free-charge density at any point in a device would be given by the material effective density of states multiplied by a half-order Fermi integral of the Fermi energy minus the conduction-band energy or

$$n_{\text{free}}(z) = N_c F_{1/2}\left(\frac{E_f - E_c(z)}{kT}\right). \tag{8}$$

It can be very important to use Fermi statistics instead of Boltzmann statistics, which have been used by many authors in the past, to determine the carrier concentrations. This is because in heavily doped cases, the bands are near degenerate or degenerate, and Boltzmann statistics will overestimate the carrier concentrations. We have calculated and tabulated the half-order Fermi integral and used a look-up table in our model to facilitate the use of Fermi statistics. Equation (8) assumes that we are dealing with a three-dimensional system in which the density of states is proportional to the square root of energy above the conduction-band edge. The introduction of a potential well alters this picture. Inside of a potential well, the confinement of carriers into two-dimensional subbands changes the form of the density of states. Above the subband energy level, the density of states in a two-dimensional subband is constant with energy. However, above the confining potential, which we term E_b for the barrier energy, there will again be three-dimensional states. Instead of the conduction band defining the lower bound on the states as in a bulk semiconductor and as written in Eq. (8), now the barrier potential defines the lower bound on the freelike states. Thus, we write the freelike state density as

$$n(z) = N_c F_{1/2}\left(\frac{E_f - E_b}{kT}\right). \tag{9}$$

In a system with a flat conduction band except for a single quantum well, the value for the barrier energy would be obvious. With the potential profile of a MODFET, the choice is less clear; however, we generally used the top of the conduction-band discontinuity as the barrier energy. The new density-of-states profile is shown schematically in Fig. 3. Here, we show two confined subbands and free states at an energy above the confining potential.

In order to determine the two-dimensionally confined charge profile, one must solve the Schrödinger equation for the subband envelope functions and their occupations. For the n-type MODFET, this implies modeling subbands in the valence band. In this case, the one-band Schrödinger equation can be used. The Schrödinger equation must, in general, be written in three dimensions, and the effective mass will be, in general, a tensor. In the electron case, the z-dependent portion of the Schrödinger equation is strictly separable from the in-plane portion of the equation which gives us extended Bloch-like states. The one-dimensional (z-dependent) Schrödinger equation can be written using the perpendicular portion of the effective mass tensor as follows:

$$\left(-\frac{\hbar^2}{2m_\perp^*(z)}\frac{\partial^2}{\partial z^2} + V(z)\right)\phi_n(z) = E_n\phi_n(z). \tag{10}$$

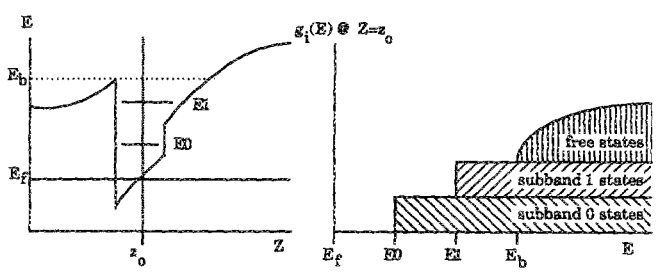

FIG. 3. Conduction-band profile and density of states at a point inside of the confining well. The free-electron states do not appear until above the confining potential.

In past studies, many authors have either made a triangular well approximation[11] or used the variational technique to fit the envelope functions.[12] However, these techniques fail in several key areas. First, a large amount of charge may penetrate into the barrier. Indeed, some of the higher-energy subbands are actually localized spatially inside of the barrier region. The triangular well approximation completely ignores the effect of the confined charge extending into the barrier. The shape of the potential profile in the barrier can vary dramatically for different doping profiles. This causes the wave functions to take on many diverse forms, especially in the barrier portion of the device. Because the wave functions can take on many different forms, picking generalized equations becomes very difficult, if not impossible, and thus the variational method becomes extremely difficult to use. In addition to this, it can be quite important to include the effect of different effective masses in different material layers in the formalism. Neither the variational technique nor the triangular well approximation is capable of dealing with effective mass variations. Because of these constraints, we have used a numerical finite-difference technique to solve the Schrödinger equation. This technique is capable of correctly solving for the wave functions in an arbitrarily shaped potential profile and also of modeling different effective masses in different material layers.

Once the Schrödinger equation has been solved for the envelope functions and the subband energy levels, it is straightforward to calculate the subband occupations. Since the subband density of states is constant with energy, the occupation comes from a first-order Fermi integral which is analytically integrable. In the electron case, we can write the occupation as

$$n_i = \frac{m_\parallel^*}{\pi\hbar^2} kT \ln\left[1 + \exp\left(\frac{(E_i - E_F)}{kT}\right)\right]. \tag{11}$$

The only complication in evaluating this equation is to choose the proper value for the effective mass. If the wave function extends into regions of different effective mass, then the value used in Eq. (11) must be weighted by the probability function over the masses in the different layers. In general, the subband density-of-states effective mass will be different for each subband.

The last parameter which is of importance is the band offsets at the heterojunctions. Our model simply incorporates measured values for these parameters. For the AlGaAs-GaAs heterointerface, most people agree that the conduction-band offset is approximately 70% of the bandgap difference.[13] For the AlInAs-InGaAs heterointerface lattice matched to InP, the conduction-band offset is closer to 75%.[14] When modeling the discontinuity for pseudomorphically strained heterointerfaces, we assume that the percent of the discontinuity in the conduction band remains the same as it is in the lattice-matched heterointerface. The absolute value of the discontinuity then changes with the change in the band gaps of the materials, which we calculate with the tight-binding method as mentioned above.

The formalism for modeling the *p*-type MODFET is conceptually similar, but much more complicated numerically. The complication arises out of the fact that we cannot make an effective-mass approximation for the hole bands but must instead represent the hole bands with a matrix Hamiltonian capable of describing the full hole band structure in the presence of strain and quantum confinement. We use a Kohn–Luttinger Hamiltonian for this purpose. Thus in place of Eq. (10), we write

$$\begin{bmatrix} H_{\rm hh} & c & b & 0 \\ c^* & H_{\rm lh} & 0 & -b \\ b^* & 0 & H_{\rm lh} & c \\ 0 & -b^* & c^* & H_{\rm hh} \end{bmatrix} \begin{bmatrix} a_n(\mathbf{k}_\parallel,z) \\ b_n(\mathbf{k}_\parallel,z) \\ c_n(\mathbf{k}_\parallel,z) \\ d_n(\mathbf{k}_\parallel,z) \end{bmatrix} = E_n \begin{bmatrix} a_n(\mathbf{k}_\parallel,z) \\ b_n(\mathbf{k}_\parallel,z) \\ c_n(\mathbf{k}_\parallel,z) \\ d_n(\mathbf{k}_\parallel,z) \end{bmatrix} \tag{12}$$

where the elements of the Kohn Luttinger Hamiltonian are given by

$$\begin{aligned} H_{\rm hh} &= -\frac{\hbar^2}{2m_0}\left((k_x^2 + k_y^2)(\gamma_1 + \gamma_2) - (\gamma_1 - 2\gamma_2)\frac{\partial^2}{\partial^2 z}\right) \\ &\quad + V(z) + \tfrac{1}{2}\delta_{\rm sh}, \\ H_{\rm lh} &= -\frac{\hbar^2}{2m_0}\left((k_x^2 + k_y^2)(\gamma_1 - \gamma_2) - (\gamma_1 + 2\gamma_2)\frac{\partial^2}{\partial^2 z}\right) \\ &\quad + V(z) - \tfrac{1}{2}\delta_{\rm sh}, \\ c &= \frac{\sqrt{3}\hbar^2}{2m_0}\left[\gamma_2(k_x^2 - k_y^2) - 2i\gamma_3 k_x k_y\right], \\ b &= \frac{\sqrt{3}\hbar^2}{m_0}(-k_y - ik_x)\gamma_3\frac{\partial}{\partial z}. \end{aligned} \tag{13}$$

Here γ_1, γ_2, and γ_3 are the Luttinger parameters for the given material and may change as a function of z across material heterojunctions. We use the values of the Luttinger parameters given by Lawaetz.[15] The shear-strain-induced band splitting $\delta_{\rm sh}$ is given by

$$\delta_{\rm sh} = -2b[(c_{11} + 2c_{12})/c_{11}]\epsilon, \tag{14}$$

where c_{11} and c_{12} are the elastic parameters of the channel material, ϵ is the strain defined by Eq. (2), and b is a material deformation potential. The wave functions are then given by

$$\Phi_n(\mathbf{k}_\parallel,z) = \begin{bmatrix} a_n(\mathbf{k}_\parallel,z)\cdot\phi_{3/2,3/2} \\ b_n(\mathbf{k}_\parallel,z)\cdot\phi_{3/2,-1/2} \\ c_n(\mathbf{k}_\parallel,z)\cdot\phi_{3/2,1/2} \\ d_n(\mathbf{k}_\parallel,z)\cdot\phi_{3/2,-3/2} \end{bmatrix}, \tag{15}$$

where the terms like $\phi_{3/2,3/2}$ are the pure angular momentum states from the solution to the hydrogen-atom problem with spin-orbit interactions included.

As with Eq. (10) for the *n*-type MODFET, Eq. (12) is solved for the *p*-type MODFET to determine the subband energy levels and envelope functions. A big complication comes from the fact that the resulting hole bands are very nonparabolic. Because of this, Eq. (12) must be solved all throughout $\mathbf{k}_\parallel$ space. Another consequence of the bands being nonparabolic is that the density of states will not be a constant function of energy. Hence, we must get the density of states numerically. We can write g_n, the density of states in subband n, as

$$g_n(E) = \frac{1}{4\pi^2}\frac{dA_n(E)}{dE}, \tag{16}$$

where $A_n(E)$ is the area in $\mathbf{k}_\parallel$ space contained by subband n at energy E. This expression must then be numerically multiplied by the Fermi distribution function and integrated over energy to obtain the subband occupations.

III. RESULTS

The evaluation of our formalism for either n- or p-type devices accurately yields the conduction- and valence-band profiles, the charge-density profile, and the energies and occupations of the two-dimensional subbands. This information can be obtained for any given layer structure. It is quite useful to have this sort of information available when designing optimized MODFET structures.

Quite generally, the type of results which we obtain from our model for n-type MODFETs are shown in Fig. 4. This simulation was done for 300-K device operation. The figure shows the conduction- and valence-band potential profiles in a typical InAlAs-InGaAs n-type pseudomorphic MODFET and the charge distribution in the same device. From the two humps in the shape of the quantum confined charge profile shown in the figure, it can be seen that there are subband states spatially localized in the barrier as well as in the channel. The effect of the strain on this device was to create a larger conduction-band discontinuity between the barrier and channel, and to create a deeper potential well in which the electrons are contained. This tends to improve both the spatial and energetic confinement of the subbands.[16]

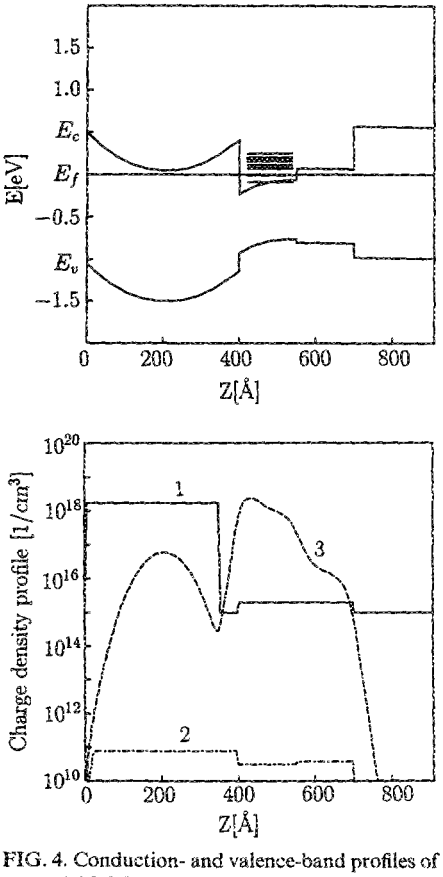

FIG. 4. Conduction- and valence-band profiles of a typical pseudomorphic n-type MODFET built on an InP substrate and the (1) doping, (2) free, and (3) quantum-confined charge-density profiles in the device.

The effects of varying strain in the channel of an n-type MODFET are shown in Fig. 5. This figure shows the sheet charge for a series of n-type MODFETs grown on an InP substrate. The left-most point on the curves is for a lattice-matched MODFET with an $In_{0.53}Ga_{0.47}As$ channel. In each device, the well width was chosen to be just under the critical thickness for its channel composition. As can be seen, increasing the strain yields a steady increase in the total sheet charge concentration. This is due to the increased band discontinuity between the barrier and well. The other information which is apparent from the figure is the greatly increased confinement. In the unstrained MODFET, only around 65% of the sheet charge is in the ground state. As we go to very large strains, almost all of the charge is localized in the lowest-energy subband. This improvement in confinement is due to the ground state falling into a deep quantum well created by a thin layer of highly strained material. Since the well becomes narrower and deeper with increased indium composition of the channel, the energy separation between the ground and first excited states becomes larger and larger. This has significant implications for mobility because of the decreased scattering and the lower effective mass of particles in the ground state. Theoretical work by Mori and Ando[17] has shown that the mobility in the ground state of a quantum well will be several times less than that of even the first excited state. We feel that much of the observed improvement in the characteristics of pseudomorphic n-type MODFETs may be due to better confinement of the carriers and, hence, higher mobility.

Based on the results of Fig. 5 and Table II, our calculations would suggest that pseudomorphic n-MODFET performance would improve monotonically with increased indium content. However, it must be realized that there may be additional effects arising from the quality of strained layer interfaces which need to be understood to fully realize this potential. While lattice-matched heterojunctions can now be

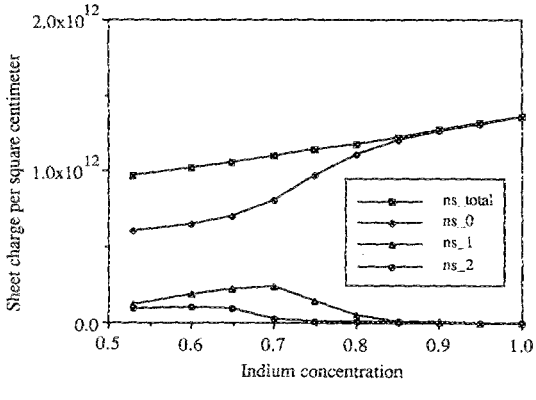

FIG. 5. Total sheet charge and charge in the ground and first two excited states as a function of indium composition in a n-type pseudomorphic MODFET. The left-most points on the curve correspond to a $In_{0.53}Ga_{0.47}As$ channel which is lattice matched to the substrate. Note that as the strain increases, the total sheet charge increases as well as does the confinement in the ground-state subband. The strained well width for each point was chosen to be just under the critical thickness for the well composition as listed in Table I.

grown with one-monolayer interface fluctuations, it is not clear if highly strained interfaces will be of similar quality.

Figure 6 shows the valence-band profile for a lattice-matched and a pseudomorphic p-type AlGaAs-GaInAs-GaAs MODFET and their associated hole subband dispersions. The pseudomorphic MODFET simulated had 12% indium in the channel. The dashed lines in the conduction band on the pseudomorphic case come from the splitting of the light- and heavy-hole bands caused by the shear component of the biaxial strain in the pseudomorphic layer. This splitting raises the $\phi_{3/2,3/2}$ state above the $\phi_{3/2,1/2}$ state in energy. The magnitude of the splitting is given by Eq. (14). In the in-plane directions, the $\phi_{3/2,3/2}$ state is significantly lighter than the $\phi_{3/2,1/2}$ state. Thus, the in-plane effective mass, which is the important mass for transport parallel to the layers, can be much lower then the normal hole effective masses. This shows up in Fig. 6 as a very high curvature in the energy-momentum subbands. At room temperature, our simulation gave the average in-plane effective mass of the hole bands as $0.56m_0$ for the lattice-matched p-type MODFET and $0.32m_0$ for the pseudomorphic p-type MODFET. At lower temperatures, this effect is even more pronounced. This is because the low-temperature distribution function pushes the holes to the tops of the subbands. In the lattice-matched case, the tops of the subbands have about the same mass as the rest of the bands, and thus the mass does not significantly change. In the strained p-type MODFET, the tops of the bands are very light. At 77 K, the effective mass of the hole gas is $0.58m_0$ for lattice-matched MODFET and $0.15m_0$ for the pseudomorphic MODFET.

With the addition of even greater amounts of indium into the channel of the MODFET, the larger strains bring about larger band splittings which cause the masses to become even lighter. Masses approaching that of the electron effective mass can be achieved. Figure 7 shows the calculated room-temperature effective hole masses for a series of pseudomorphic p-type MODFETs with different channel compositions. As in Fig. 5, the well width in each of these devices was chosen be just under the critical thickness for the given channel composition. As can be seen from the figure, the hole mass for an unstrained MODFET is even higher than the hole mass in a bulk crystal, which is around $0.34m_0$. This is due to the coupling of the bands in the quantum confinement. Thus, we can see the very significant decrease in effective mass which is brought about by the decoupling of the light- and the heavy-hole states due to the strain in the system. As is shown in the figure, the hole effective mass can be reduced by more than a factor of 4. Significantly, much of this decrease can be achieved with the modest strains present in $In_{0.20}Ga_{0.80}As$, which is not as difficult to grow as more highly strained materials. The masses given here are in-plane density-of-states effective masses averaged over the entire hole gas. A more detailed description of the effect of strain on the masses in each of the subbands has recently been published by the authors.[18]

Some attention has been given recently to the concept of delta-doped MODFET structures.[19] Delta doping entails placing a very high concentration of donor atoms in a very narrow layer close to the heterojunction as opposed to distributing the donors over a thicker layer between the heterointerface and gate. Using growth-interruption techniques, this concept has been taken to its extreme by placing all of the donors into a single monolayer. Since a large variety of structures of this type have been proposed, we decided to examine the advantages and disadvantages of the concept of delta doping. In order to assess the effects of the doping distribution, we performed a series of simulations on a typical n-type pseudomorphic device structure. We varied the

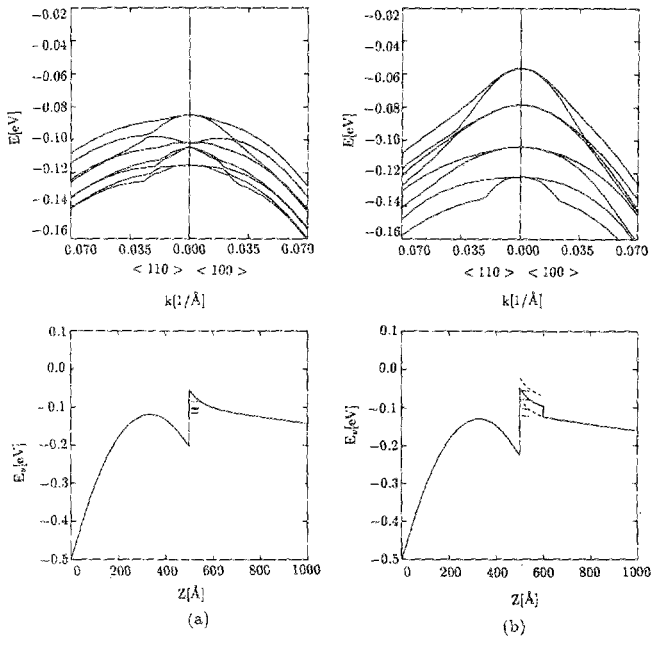

FIG. 6. Valence-band profile of (a) a lattice-matched and (b) a pseudomorphic p-type MODFET and the in-plane dispersion curves of the hole subbands. The dashed lines in the valence band indicate the effective valence-band profile for the light and the heavy holes which have been split by strain. Note the high curvature of the subbands, indicating a low effective mass in the pseudomorphic MODFET.

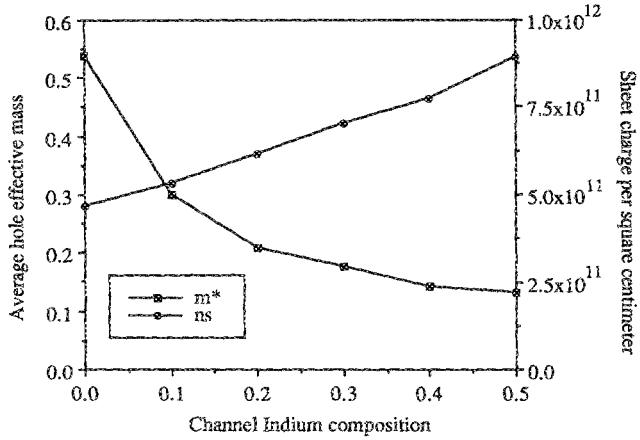

FIG. 7. Averaged hole gas effective mass as a function of indium composition in the channel. The zero indium device is lattice matched to the GaAs substrate and has very heavy hole bands because of the coupling between the light- and heavy-hole states. The addition of strain greatly reduces the effective mass in the hole bands. Also shown is the sheet charge density of each device. As the well becomes deeper as a result of the increased strain, the sheet charge increases. The strained well width for each point was chosen to be just under the critical thickness for the well composition as listed in Table I.

doping distribution within the barrier of the device; however, a 50-Å undoped spacer layer between the heterointerface and donors was maintained. In our simulations, we varied the width of the doped region from spike directly up against the undoped spacer layer all the way up to a uniform doping between the gate and spacer. Initially, we varied the doping concentration in order to keep the sheet-doping dose, or the donor concentration per cubic centimeter multiplied by the thickness of the doped layer, a constant. Keeping the doping dose constant facilitated a study of the doping transfer efficiency, or the percentage of the donated electrons which transfer into the channel, as a function of the doping profile.

In performing these simulations, we found that it was very important to include the effect of donor ionization and to provide an accurate value for the donor energy level. This is because, in the cases where the doping region was thin, the doping concentration gets very high. If the approximation is made that all donors are ionized, which many authors have made in previous studies, this high doping concentration will cause the conduction band to pass significantly below the Fermi energy.[20] In this case, we can be certain that many of the donors will not be ionized. The effect of including donor ionization in the model is to prevent the conduction band from becoming degenerate. This implies, in general, that the calculated sheet charge will be lower than it would have been if it was assumed that all of the donors were ionized. In the simulations presented here, we assume that the $In_{0.52}Al_{0.48}As$ is silicon doped with a donor binding energy of 6 meV.

Figure 8 shows the conduction-band profile, the squared magnitudes of the first ten subband wave functions, and the quantum-confined charge profile in a pseudomorphic MODFET where all of the dopants are in a 10-Å-thick layer immediately on top of the spacer. Figure 9 shows the same information for a device where the same dose of donors are spread out over the entire region between the gate and spacer. Several interesting features of the two figures become evident. By examining the wave functions, one can see that some of the energy levels of the system are spatially localized within the barrier. This is more pronounced in the spread-doping case (Fig. 9), because the "potential well" in the barrier is further from the potential well in the channel. Thus, the third excited state of the system, ϕ_2 in Fig. 9, resembles a groundlike state spatially confined inside the barrier. In actuality, there are three humps to this curve as it is the excited state of the system; however, two of them are too small to be seen on the scale shown. Overall, the total charge in the barrier is significantly higher in the delta-doped case than in the spread-doped case. For the devices which we simulated and picture in Figs. 8 and 9, there is more than 3 times as much charge in the barrier in the delta-doped case then in the spread-doped case. In MODFET design, it is best to avoid charge in the barrier because of the lower carrier

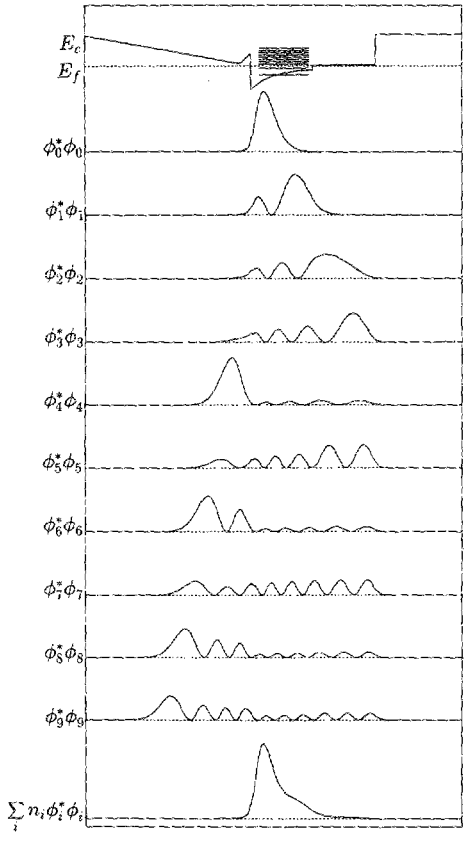

FIG. 8. Conduction-band profile, squared magnitudes of the first ten wave functions, and the quantum-confined charge profile in a delta-doped MODFET.

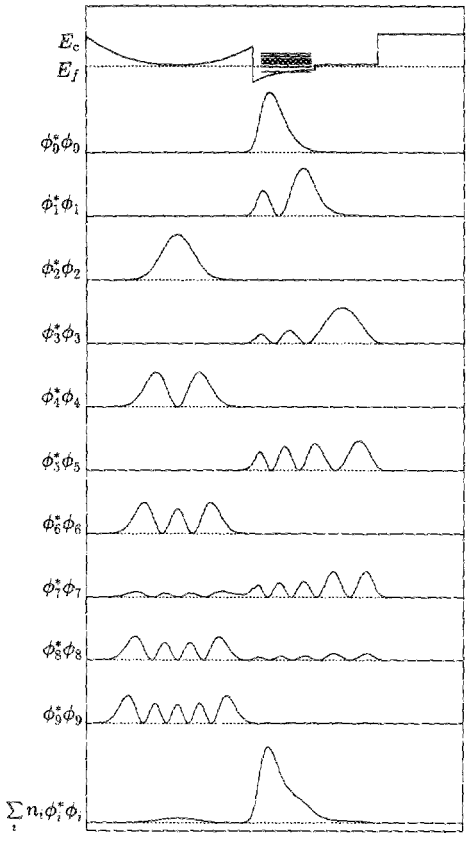

FIG. 9. Conduction-band profile, squared magnitudes of the first ten wave functions, and the quantum-confined charge profile in a spread-doped MODFET.

velocity in the barrier material and, therefore, the inferior MODFET transconductance. While these carriers could be depleted out of the barrier by lowering the gate voltage, this would lower the sheet charge concentration. The simulations show that in order to get the same large sheet charge concentrations in the channel which the delta-doped MODFET is capable of, the spread-doped MODFET needs to have significant charge in the barrier as well.

As mentioned before, the doping dose was kept constant as the width of the doped region was varied as in Figs. 8 and 9. However, the sheet charge in the delta-doped case is higher than in the spread-doped case. This implies that there is a greater transfer efficiency of donated electrons from the donors into the channel. This trend is demonstrated in Fig. 10, which shows the sheet charge in the channel as a function of the doping width. The figure shows that there is a steady increase in the transfer efficiency as the donors are brought closer and closer to the channel. Also shown in the figure is what the curve would look like if all of the donors were ionized. As can be seen, this would overestimate the channel charge significantly in the delta-doped case.

Because the conduction band in the delta-doped MODFET will be lower near the heterojunction, the delta-doped MODFET can achieve a greater maximum sheet charge than the spread-doped MODFET. The sheet charge density, however, is limited by the donor-binding level. Once the conduction band falls to within the donor-binding level of the Fermi energy, the donor states will start to fill, and past that point, increasing the doping will not increase the sheet charge further. The increase in transfer efficiency, demonstrated in Fig. 10, will also be affected by donor ionization, and thus the improvement demonstrated in Fig. 10 will only be observed at low or moderate doping doses. When a spread-doped MODFET is over doped, the conduction band from the gate all the way to the spacer will lower towards the Fermi energy, and there will be an extremely large barrier charge. In this case, the barrier charge acts as a parasitic MESFET in which the carriers will have low mobility as a result of the high scattering rate in the presence of the donors and the high effective mass in the barrier region which contains aluminum. When a delta-doped MODFE is overdoped, the effect on the zero-bias bands is less obvio since the conduction band at the doping spike was alreac close to degenerate, and the donor ionization effect will pr vent the conduction band from getting much closer to th Fermi energy than the donor-binding energy. Howeve overdoping a delta-doped MODFET will have an advers effect on the transconductance and may adversely affect th high-frequency characteristics because of the time constan associated with the donor states.

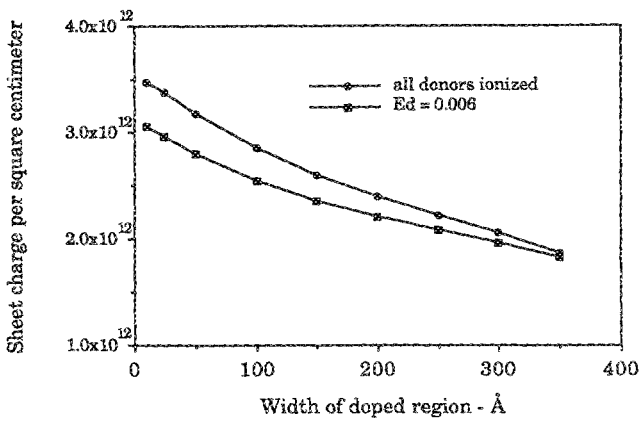

FIG. 10. Two-dimensional sheet charge in a MODFET as a function of the width of the doped region for a constant doping dose. Shown is a curve calculated assuming that the donor binding energy is 6 meV and another curve calculated assuming that all donors are ionized. As can be seen, the assumption that all donors are ionized overestimates the charge density in the device.

We next examined the effect of doping distribution on transconductance or the gate's control over the channel charge. We examined the effect of gate voltage in two systems. The first had a doping width of 350 Å and a doping concentration of 1.148×10^{18} cm^{-3}, or a doping dose of 4.0×10^{12} cm^{-2}. This device had a zero-bias channel sheet charge density of 1.5×10^{12}cm^{-2}. In order to compare the transconductance, we simulated a delta-doped structure with a lower doping dose in order that the sheet charge concentration at zero gate bias be the same. The delta-doped device we simulated had a doped region width of 10 Å and a doping density of 1.37×10^{19} cm^{-3} or a doping dose of 1.37×10^{12} cm^{-2}. Figure 11 shows the sheet charge density in the channel of each of the devices as a function of gate bias. As can be seen, the spread-doped device and the low-dose delta-doped devices have very similar characteristics except near cutoff. Here, the delta-doped device exhibits inferior performance as the channel does not turn off as hard off as it does in the spread-doped device. The lack of a hard pinch off is due to the fact that the conduction band passes below the Fermi energy and thus a significant portion of the donors in the delta-doped MODFET are not ionized when the gate is biased at 0 V. As the gate voltage is decreased and the conduction band is pulled up, more of the donors ionize. When the gate voltage gets low enough for all of the donors to ionize, the channel does pinch off completely.

The delta-doped MODFET has a possible additional advantage in lower gate leakage. This can take on great importance since gate current can plague the performance of MODFETs, especially *p*-type devices.[6] A spread-doped MODFET which is doped high enough to produce a high sheet charge, on the order of 3×10^{12}/cm^2, will have a very

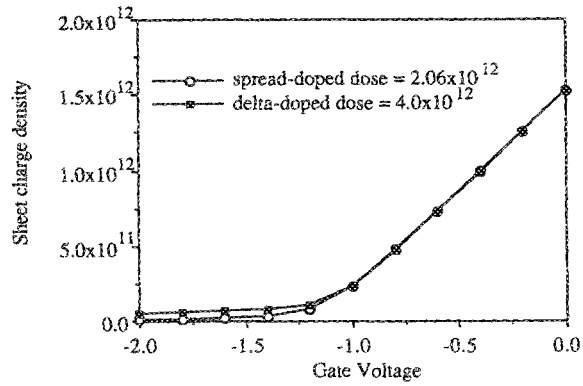

FIG. 11. Sheet charge density as a function of gate voltage for a delta-doped and a spread-doped MODFET. The doping dose for the delta-doped MODFET is lower so that the sheet charge at zero bias for the two devices is the same. The two curves are similar except near cutoff.

high slope to the conduction band directly beneath the Schottky barrier. The conduction band of such a device is shown in Fig. 4. Because of the steep descent of the conduction band, carriers will be more likely to tunnel into the barrier from the gate. Additionally, gate current may be enabled by the donors in the spread-doped device which provide an alternate route for gate conduction as a result of hopping through deep levels associated with donors in the barrier. Although it would be very difficult to estimate the magnitudes of these effects, it is clear that the delta-doped MODFET will exhibit superior performance.

IV. CONCLUSION

We have developed an accurate formalism for the simulation of *n*- and *p*-type lattice-matched and pseudomorphic MODFETs. Our model is versatile enough to handle a variety of different structures and situations including spread and delta doping, overdoping, and pseudomorphic effects. Our model predicts that pseudomorphic *n*-type MODFETs will have increased sheet charge densities and improved carrier confinement over lattice-matched *n*-type MODFETs because of a higher conduction-band offset and a deeper potential well. For pseudomorphic *p*-type MODFETs, our model predicts significantly lower hole effective masses than in lattice-matched *p*-type MODFETs because of the decoupling of the light- and heavy-hole subbands. We have used our model to investigate the differences between spread-doped and delta-doped MODFETs. We find that there is a greater transfer efficiency in the delta-doped MODFET than in the spread-doped MODFET, and the maximum sheet charge obtainable is higher in a delta-doped MODFET. We also find that for devices doped so as to have the same channel carrier concentration, the transconductance properties are similar except in cutoff where the delta-doped MODFET shows inferior performance. The delta-doped MODFET may significantly help to solve the gate leakage problems due to reduced tunneling and fewer gap states available for conduction. We also find that because of similar static, zero-bias conduction-band profiles, the over doping of a delta-doped MODFET may be difficult to detect by dc measurements like Hall characterization and velocity field profiling. However, because of the donor time constant we feel that is possible that such overdoped delta-doped MODFETs may exhibit inferior high-frequency performance. It is clear that pulse doping can provide another variable for optimizing device performance, and the formalism presented can be a useful tool for this optimization.

ACKNOWLEDGMENTS

This work was supported by the National Science Foundation and the Materials Research Group program and by the U.S. Army Office (Grant No. DAAL03-87-U-007). One of us (M. J.) gratefully acknowledges the generous support of the Eastman Kodak Company.

[1]M. Nathan, M. Heiblum, J. Klem, and H. Morkoç, J. Vac. Sci. Technol. B **2**, 167 (1984).
[2]A. Ketterson, W. Masselink, J. Gedymin, J. Klem, C. Peng, W. Kopp, H. Morkoç, and K. Gleason, Trans. Electron Devices **33**, 564 (1986).
[3]E. Jones, I. Fritz, J. Schirber, M. Smith, and T. Drummond, in Proceedings of the International Symposium of GaAs and Related Compounds, 1986, p. 227.
[4]J. Hinckley and J. Singh, Appl. Phys. Lett. **53**, 785 (1988).
[5]T. Drummond, T. Zipperian, I. Fritz, J. Schirber, and T. Plut, Appl. Phys. Lett. **49**, 461 (1986).
[6]C. Lee, H. Wang, G. Sullivan, N. Sheng, and D. Miller, IEEE Electron Device Lett. **EDL-8**, 85 (1987).
[7]C. Kuo, S. Vong, R. Cohen, and G. Stringfellow, J. Appl. Phys. **57**, 5428 (1985).
[8]P. Szydlik, S. Alterovitz, E. Haugland, B. Segall, T. Henderson, J. Klem, and H. Morkoç, Superlatt. Microstruct. **4**, 619 (1988).
[9]M. Jaffe and J. Singh, Solid State Commun. **62**, 399 (1987).
[10]G. Norris, D. Look, W. Koop, J. Klem, and H. Morkoç, Appl. Phys. Lett. **47**, 423 (1985).
[11]D. Delagebeaudeuf and N. Linh, IEEE Trans. Electron Devices **ED-29**, 955 (1982).
[12]A. Petelin, F. Crowne, S. Duncan, and B. Beack (unpublished).
[13]D. Wolford, T. Kuech, J. Bradley, M. Gell, D. Ninno, and M. Jaros, J. Vac. Sci. Technol. B **4**, 1043 (1986).
[14]C. Peng, A. Ketterson, H. Morkoç, and P. Solomon, J. Appl. Phys. **60**, 1709 (1986).
[15]P. Lawaetz, Phys. Rev. B **4**, 3460 (1971).
[16]M. Jaffe, Y. Sekiguchi, J. East, and J. Singh, Superlatt. Microstruct. **4**, 395 (1988).
[17]S. Mori and T. Ando, J. Phys. Soc. Jpn. **48**, 8655 (1980).
[18]M. Jaffe, Y. Sekiguchi, and J. Singh, Appl. Phys. Lett. **51**, 1943 (1987).
[19]E. Schubert, J. Cunningham, W. Tsang, and G. Timp, Appl. Phys. Lett. **51**, 1170 (1987).
[20]T. Henderson, U. Reddy, G. Ji, H. Morkoç, and N. Otsuka, Int. Electron Devices Meeting Tech. Dig. **17.3**, 418 (1987).